Anion-Sublattice Engineering of Li_3PS_4: Br and I Incorporation Enhances Ionic Conductivity and Li-Metal Compatibility

Tej P. Poudel,[1,2,3,$] Michael J. Deck,[2,3,$] Ifeoluwa Peter Oyekunle,[2,3] Pawan K. Ojha,[2,3] Bright Ogbolu,[2,3] Islamiyat Ojelade,[2,3] Thilina N.D.D. Gamaralagale,[2,3] Erica Truong,[2,3] Yongkang Jin,[2,3] Amirhossein Zareihassangheshlaghi,[2] Yan-Yan Hu[1,2,3*]

1. Materials Science and Engineering Program, Florida State University, Tallahassee, FL 32310, USA
2. Department of Chemistry and Biochemistry, Florida State University, Tallahassee, FL 32306, USA
3. Center for Interdisciplinary Magnetic Resonance, National High Magnetic Field Laboratory, Tallahassee, FL 32310, USA

[$]*These authors contributed equally*

Supporting Information

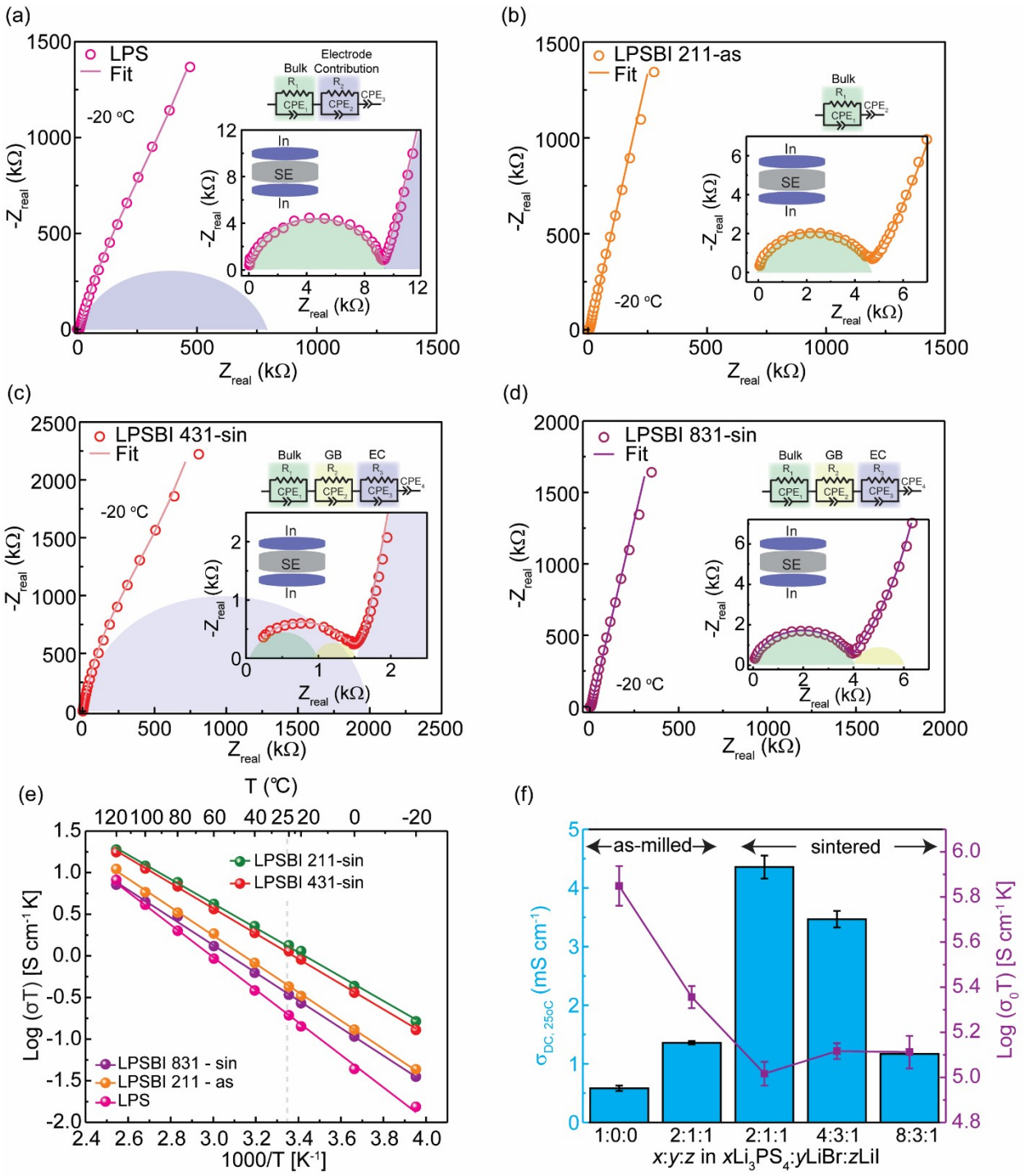

Figure S1 EIS analysis of xLi$_3$PS$_4$:yLiBr:zLiI. (a-d) Nyquist plots and the corresponding electrochemical circuit fitting of LPS, LPSBI-as, LPSBI 431-sin, and LPSBI 831-sin. Two semicircles for impedance response are observed, and the Nyquist plot is fitted with the R/Q+R/Q+Q type equivalent circuit. The high-frequency semicircle is attributed to the impedance response from the bulk of SE. The low-frequency semicircle corresponds to an electrode

contribution with a capacitance on the order of μF. (e) Arrhenius plots of corresponding SEs, the gray dashed line is a visual guide for conductivity at 25 °C. (f) Ionic conductivity and Arrhenius prefactor of different samples prepared with different strategies.

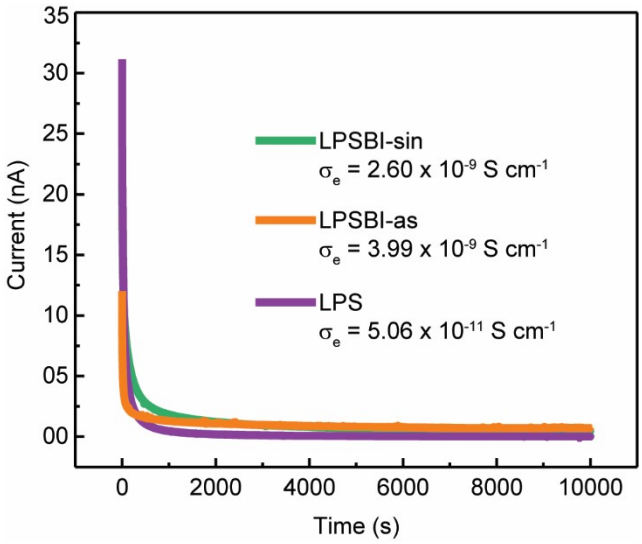

Figure S2. The DC polarization current *vs.* time plot using 0.1 V to determine the electronic conductivity of LPS, LPSBI-as, and LPSBI-sin solid electrolytes.

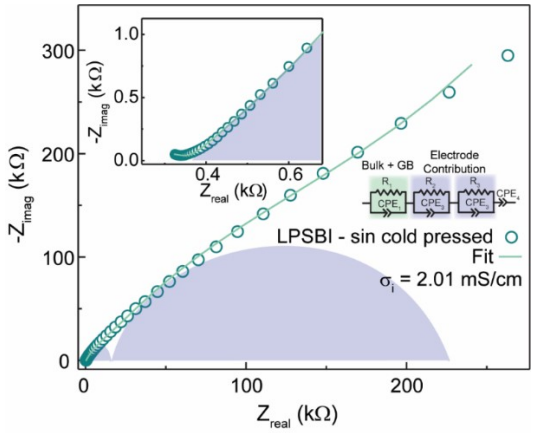

Figure S3. Nyquist plot and equivalent circuit fitting of the LPSBI – sin after grinding the pellet into powder and cold pressing again. The three semicircles were observed, with the middle- and low-frequency semicircles assigned to electrode contributions with capacitances of 0.31 μF and 0.21 μF, respectively. The high-frequency semicircle is assigned to both bulk and grain boundary contributions with a capacitance of 5.8×10^{-10} F.

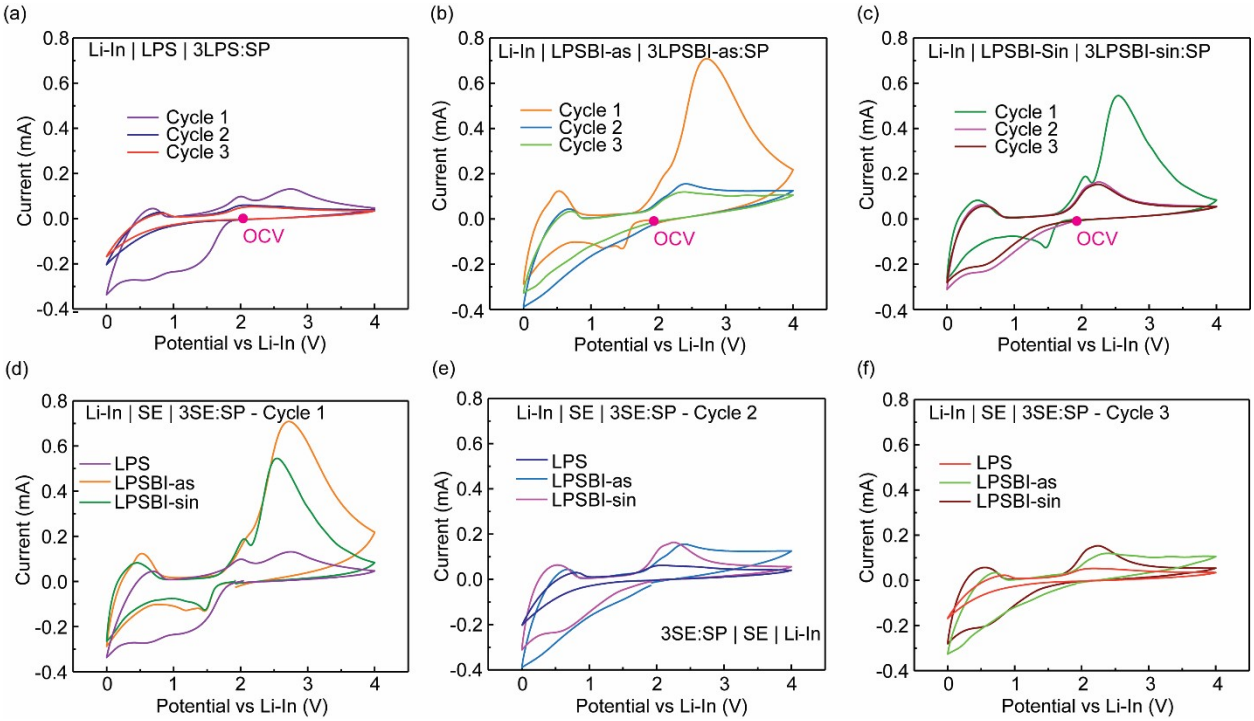

Figure S4. Cyclic voltammetry measurement of (a) LPS, (b) LPSBI-as, (c) LPSBI-sin. (d,e,f) show the comparison of the CV profiles of the three SEs for Cycles 1- 3.

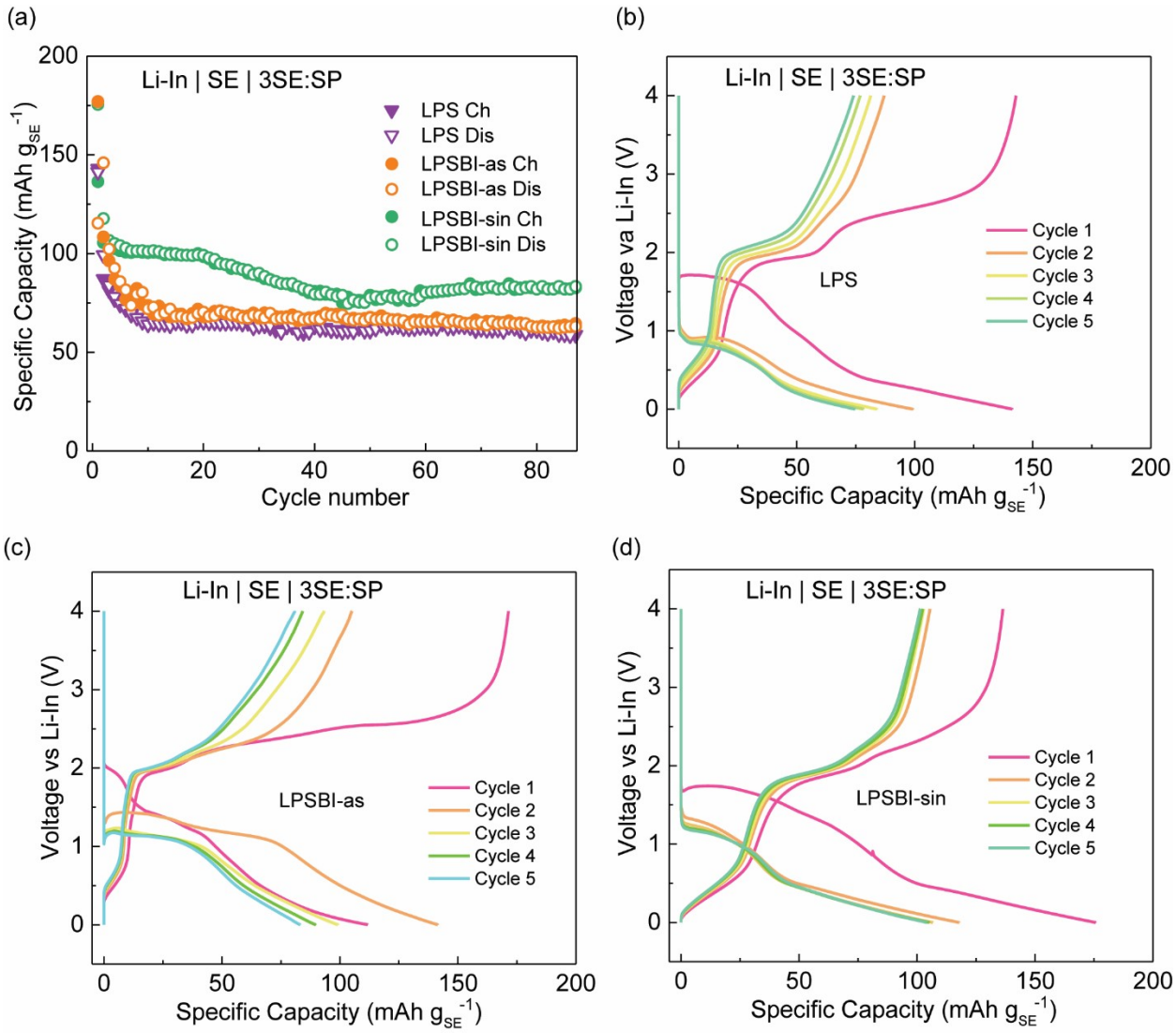

Figure S5. Galvanostatic cycling of SE-SP composites to probe reversible capacities. (a) Cycle vs capacity plot for Li-In|SE|3SE:SP cell (SE: LPS, LPSBI-as, or LPSBI-sin; SP: Super P carbon). The voltage profile of the (b) Li-In|LPS|3LPS:SP, (c) Li-In|LPSBI-as|3LPSBI-as:SP, and (d) Li-In|LPSBI-sin|3LPSBI-sin:SP cells.

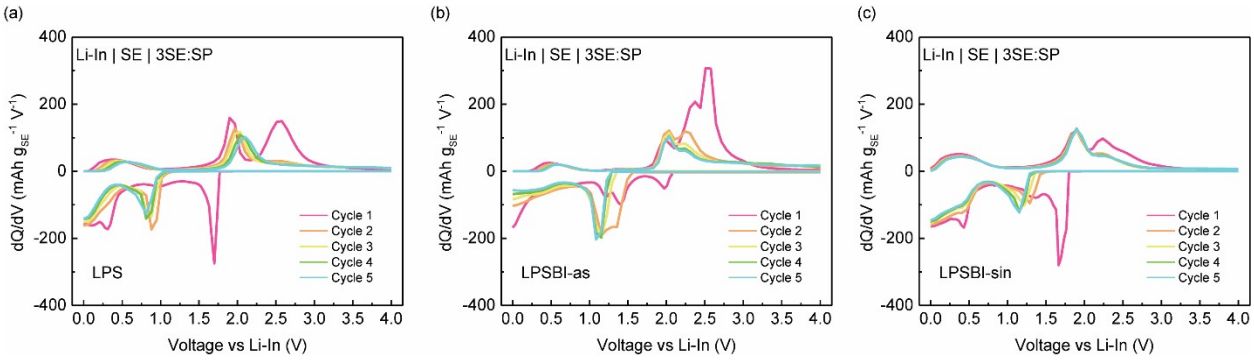

Figure S6. Differential capacity plots (a) Li-In|LPS|3LPS:SP, (b) Li-In|LPSBI-as|3LPSBI-as:SP, and (c) Li-In|LPSBI-sin|3LPSBI-sin:SP cells.

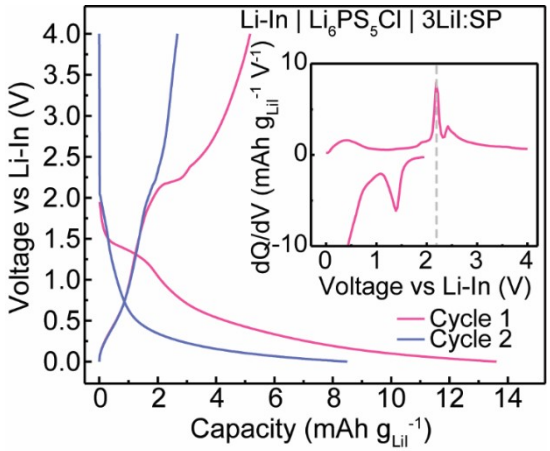

Figure S7. The voltage profile of galvanostatic cycling of 3LiI:SP catholyte to extract the information on the onset voltage of LiI oxidation. The inset shows the differential capacity of the first cycle. This LiI oxidation can be observed at an onset voltage of ~2.25 V *vs.* Li-In. This voltage is similar to the onset voltage of the extra reduction peak in the 2LPSBI–sin:TiS_2 cell, which is responsible for increased capacity up to Cycle 88.

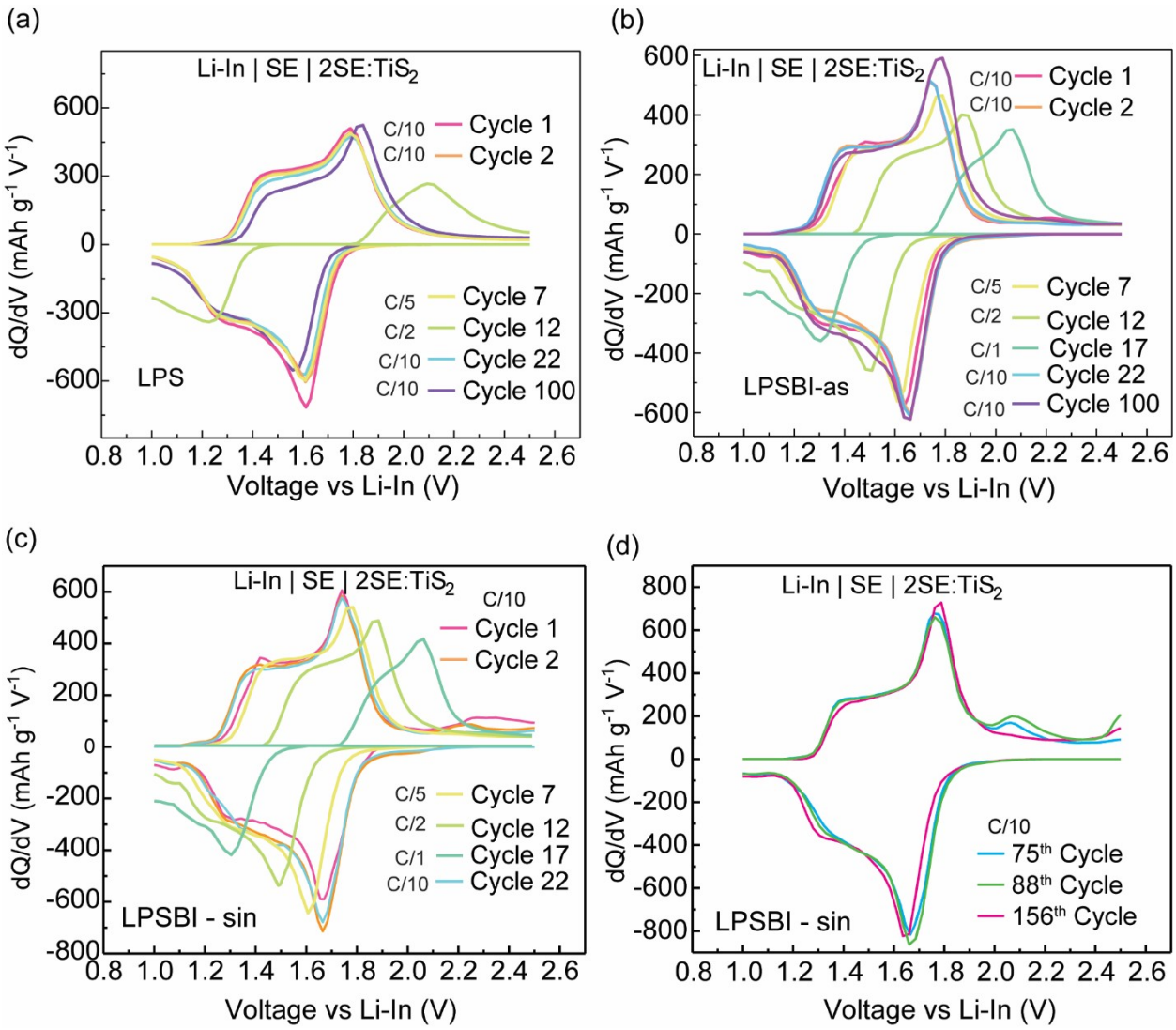

Figure S8. Differential capacities of various cycles of (a) Li-In|LPS|2LPS:TiS_2, (b) Li-In|LPSBI-as|2LPSBI-as:TiS_2, and (c,d) Li-In|LPSBI-sin|2LPSBI-sin:TiS_2

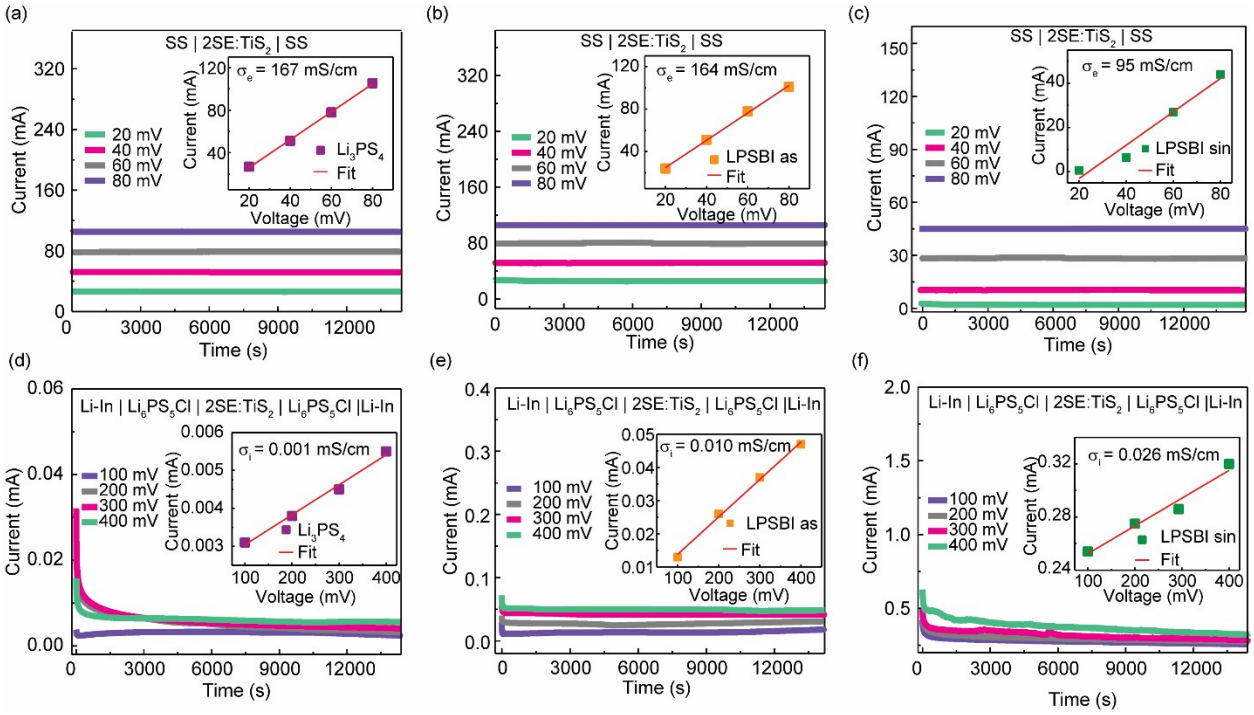

Figure S9. DC-Polarization measurements of catholytes to determine $\sigma_{e,eff}$ and $\sigma_{i,eff}$. (a-c) DC-Polarization of SS|2SE:TiS_2|SS (SE: LPS, LPSBI-as, LPSBI-sin) symmetric cells for determination of $\sigma_{e,eff,}$ and (d-f) DC-Polarization measurement of Li-In|L_6PS_5Cl|2SE-TiS_2|L_6PS_5Cl|Li-In (SE: LPS, LPSBI-as, LPSBI-sin) symmetric cells for determination of $\sigma_{i,eff}$. The insets display the respective I-V curves of the catholytes at different DC voltages with the linear fits. The electronic and ionic resistances were calculated based on Ohm's law.

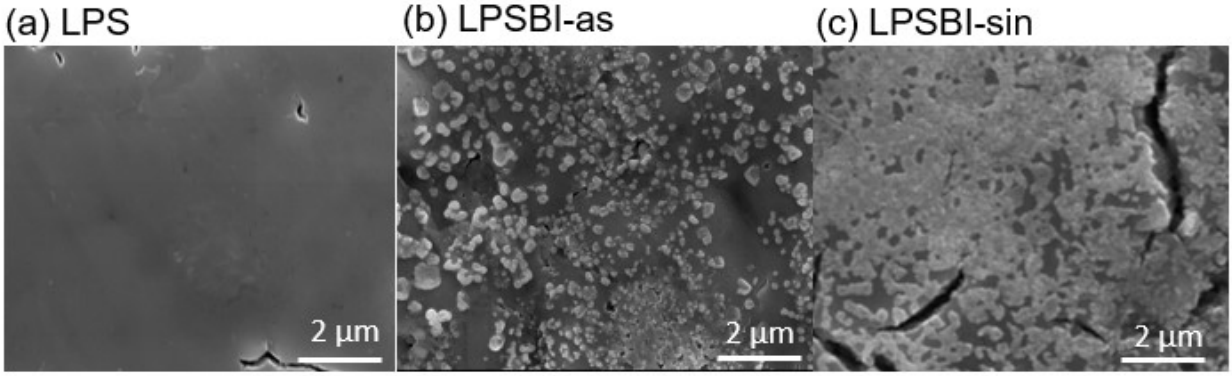

Figure S10. SEM images of (a) LPS, (b) LPSBI-as, and (c) LPSBI-sin.

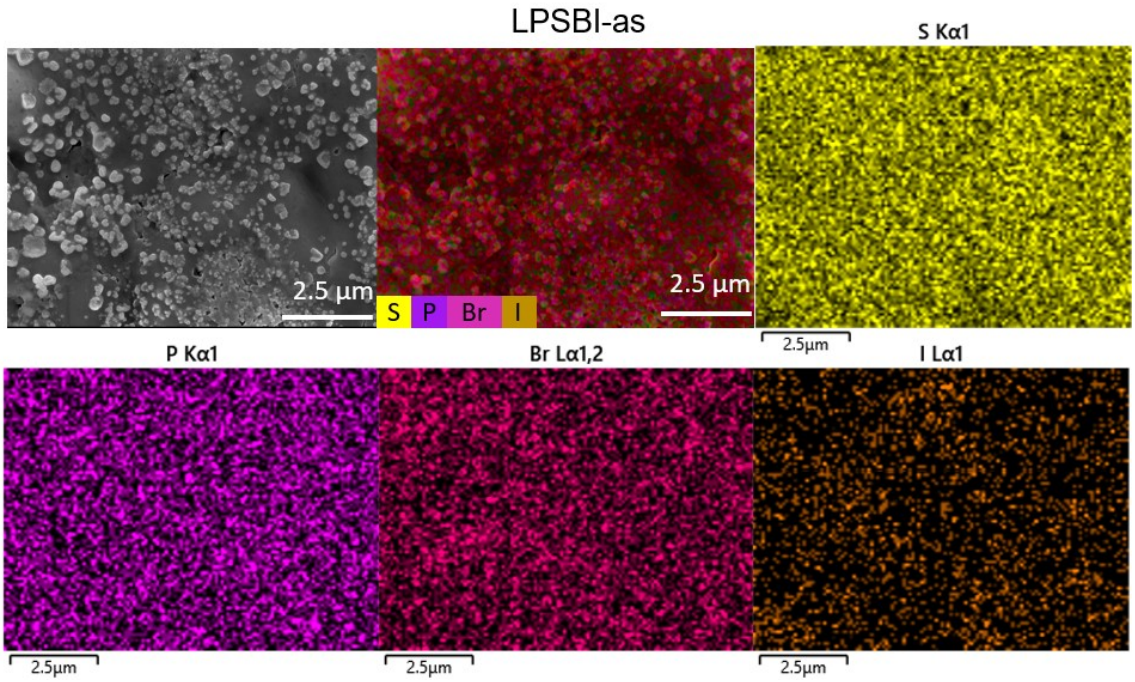

Figure S11. SEM and EDX of LPSBI-as with elemental mapping.

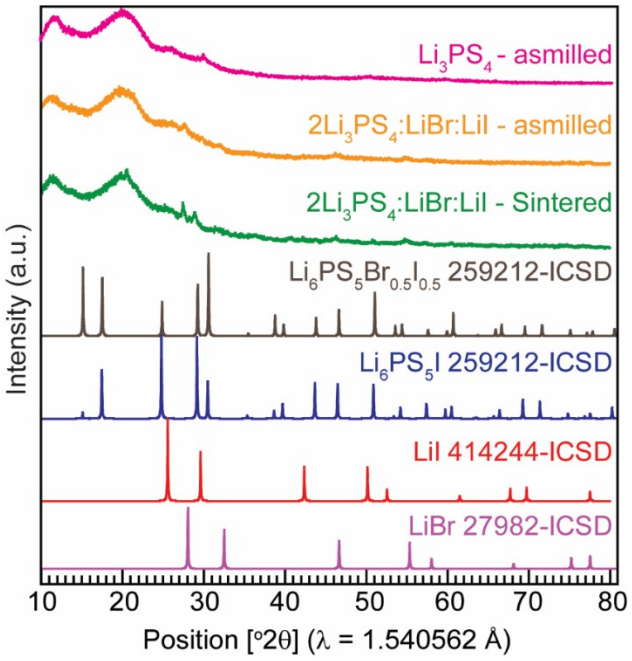

Figure S12. XRD patterns of LPS, LPSBI-as, and LPSBI-sin and comparison with reference patterns of LiBr, LiI, $Li_6PS_5Br_{0.5}I_{0.5}$, and Li_6PS_5I from ICSD.

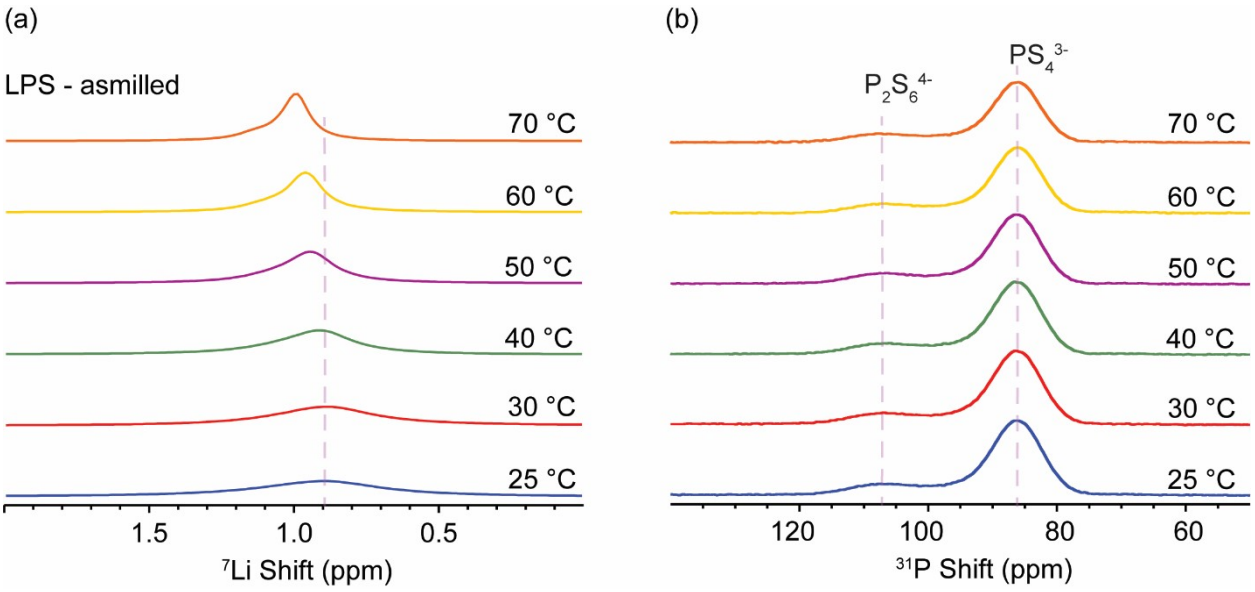

Figure S13. (a) Variable-temperature ^{7}Li MAS NMR spectra of LPS. (b) Variable-temperature ^{31}P MAS NMR spectra of LPS; the temperatures are indicated.

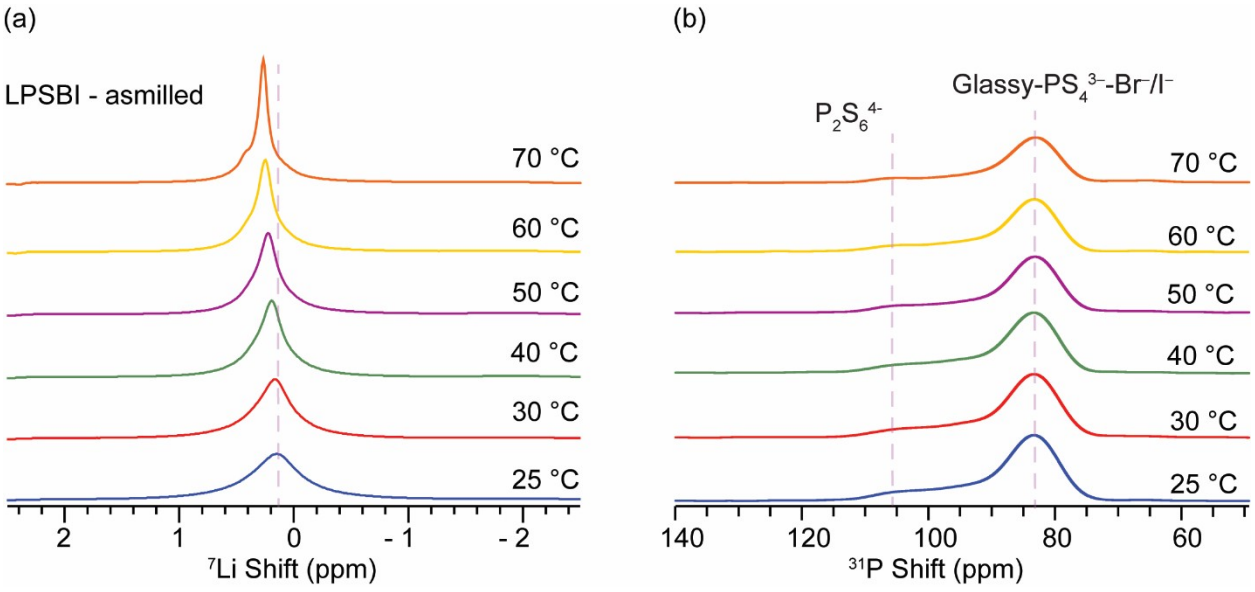

Figure S14. (a) Variable-temperature ^{7}Li MAS NMR spectra of LPSBI-as. (b) Variable-temperature ^{31}P MAS NMR spectra of LPSBI-as; the temperatures are indicated.

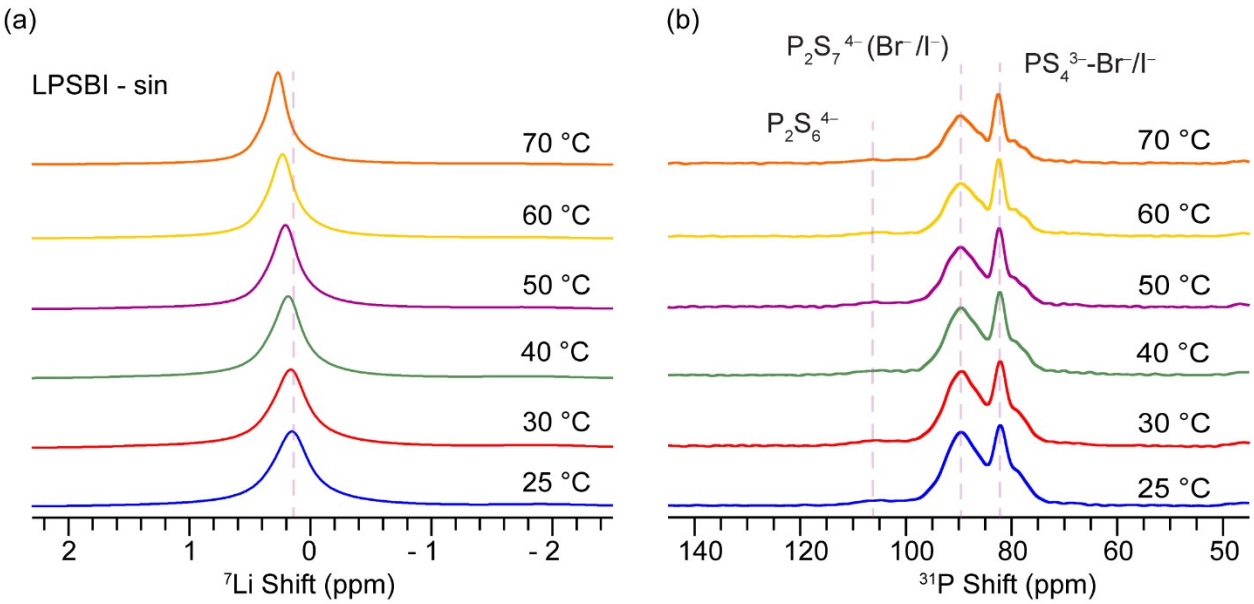

Figure S15. (a) Variable-temperature ^{7}Li MAS NMR spectra of LPSBI-sin. (b) Variable-temperature ^{31}P MAS NMR spectra of LPSBI-sin; the temperatures are indicated.

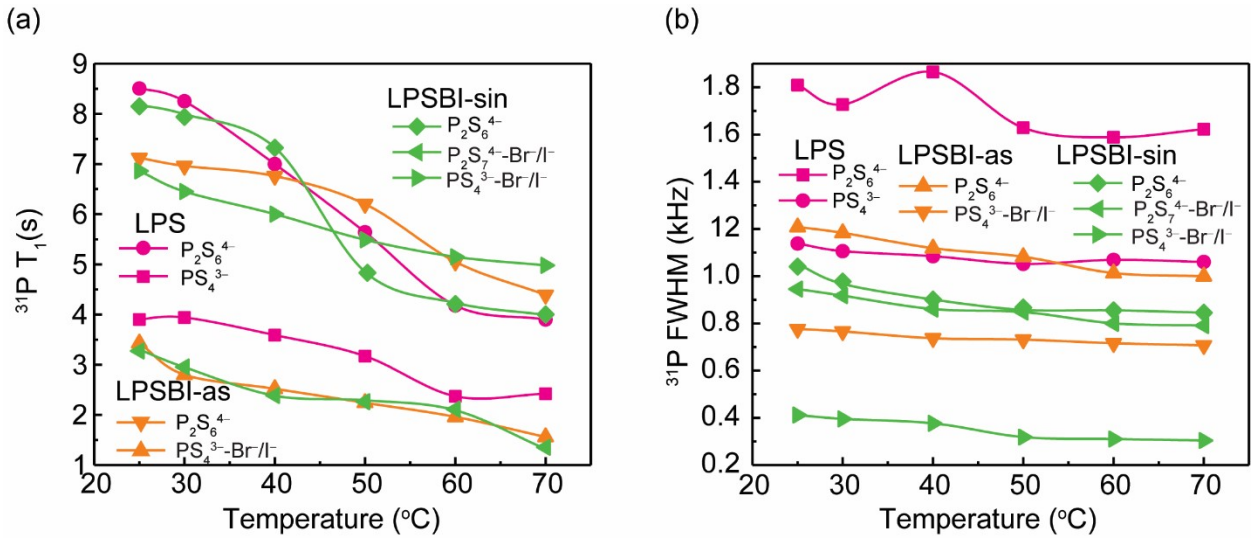

Figure S16. Variable-temperature ^{31}P NMR T_1 times for LPS, LPSBI-as, and LPSBI-sin. (d) Variable-temperature ^{31}P NMR line widths (full width at half maximum, FWHM) for LPS, LPSBI-as, and LPSBI-sin.

Table S1. The ionic conductivities of $x$$Li_3PS_4$:$y$LiBr:$z$LiI were measured at 22 °C. $2Li_3PS_4$:LiBr:LiI shows the highest conductivity of 1.36 mS/cm among the samples before sintering (LPSBI-as) and the highest conductivity of 4.36 mS/cm after sintering (LPSBI-sin) at 22 °C. This sample is selected as the model system for further characterization.

Composition	$\sigma_{DC,\ 22\ °C}$ [mS cm^{-1}]
Li_3PS_4-asmilled	0.51
Li_3PS_4:LiBr:LiI-asmilled	0.57
$2Li_3PS_4$:LiBr:LiI - asmilled	1.36
$3Li_3PS_4$:LiBr:LiI - asmilled	0.71
$3Li_3PS_4$:2LiBr:2LiI - asmilled	0.32
$4Li_3PS_4$:3LiBr:LiI - asmilled	0.91
$8Li_3PS_4$:3LiBr:1LiI - asmilled	0.69
$2Li_3PS_4$:LiBr:LiI - sintered	4.16
$4Li_3PS_4$:3LiBr:LiI - sintered	2.88
$8Li_3PS_4$:3LiBr:1LiI - sintered	1.39

Table S2. Analysis results of NMR data shown in **Figure 6 and 7**, including ^{7}Li T_1 relaxation time, line broadening, and phase fraction.

Composition	^{7}Li $T_{1,\ 22\ °C}$ [s]		Phase Quantification based on ^{6}Li NMR			
	Li1	Li2	$Li_4P_2S_6$	Li1	Li2	LiBr
LPS	1.35	0.92	-	59.3	40.7	-
LPSBI-as	1.05	0.75	-	45.7	52.6	1.7
LPSBI-sin	1.08	0.64	1.5	16.7	79.5	2.3

Table S3. NMR analysis of model samples, including line broadening, and phase fraction of different components in ^{31}P shift at 22 °C.

Composition	^{31}P Phase Quantification						
	$P_2S_6^{4-}$	$P2S_7^{4-}$ -Br^-/I^- Yellow-Green	$P2S_7^{4-}$ -Br^-/I^- Light-Green	β-PS_4^{3-} Light-Blue	Glassy-PS_4^{3-} Blue	PS_4^{3-}-Br^-/I^- Green	PS_4^{3-}-Br^-/I^- Pink
LPS	12.7	-	-	-	87.3	-	-
LPSBI-as	13.5	-	-	-	86.5	-	-
LPSBI-sin	7.8	2.6	33.4	1.8	7.2	35.6	11.6

Table S4. NMR analysis of LPS, LPSBI-as, and LPSBI-sin samples, including ^{7}Li T_1 relaxation times and linewidths at various temperatures.

	LPS		LPSBI-as		LPSBI-sin	
Temperature [℃]	^{7}Li T_1 [s]	FWHM Hz	^{7}Li T_1 [s]	FWHM Hz	^{7}Li T_1 [s]	FWHM Hz
25	1.35	54	0.98	62	0.50	48
30	1.13	45	0.96	49	0.46	39
40	0.91	33	0.77	37	0.41	32
50	0.73	24	0.63	31	0.37	23
60	0.59	18	0.52	22	0.35	22
70	0.50	12	0.42	13	0.34	18

Table S5. NMR analysis of LPS, including ^{31}P NMR T_1 relaxation time and line broadening at various temperatures.

	LPS			
Temperature [°C]	^{31}P T_1 [s]	FWHM Hz	^{31}P T_1 [s]	FWHM Hz
	PS_4^{3-}		$P_2S_6^{4-}$	
25	3.90	1138	8.51	1809
30	3.94	1106	8.25	1727
40	3.59	1084	7.00	1865
50	3.17	1052	5.64	1628
60	2.37	1069	4.18	1588
70	2.42	1060	3.90	1622

Table S6. NMR analysis of LPSBI-as, including ^{31}P NMR T_1 relaxation time and line broadening at various temperatures.

	LPSBi-as			
Temperature [°C]	^{31}P T_1 [s]	FWHM Hz	^{31}P T_1 [s]	FWHM Hz
	PS_4^{3-}-Br^-/I^-		$P_2S_6^{4-}$	
25	3.43	776	7.16	1208
30	2.80	766	6.96	1183
40	2.52	737	6.76	1118
50	2.24	731	6.20	1082
60	1.96	715	5.05	1013
70	1.56	707	4.39	999

Table S7. NMR analysis of LPSBI-sin, including ^{31}P NMR T_1 relaxation time and line broadening at various temperatures.

	LPSBI-sin					
Temperature ℃	^{31}P T_1 [s]	FWHM Hz	^{31}P T_1 [s]	FWHM Hz	^{31}P T_1 [s]	FWHM Hz
	$P_2S_7^{4-}$-Br^-/I^-		$P_2S_6^{4-}$		PS_4^{3-}-Br^-/I^-	
25	3.30	945	8.17	1050	6.86	412
30	2.95	917	7.99	967	6.45	395
40	2.38	861	7.33	901	6.00	376
50	2.29	848	4.85	857	5.49	318
60	2.09	800	4.23	855	5.15	310
70	1.32	791	3.99	845	4.98	304